

---

# UAV4D: Dynamic Neural Rendering of Human-Centric UAV Imagery using Gaussian Splatting

---

Jaehoon Choi<sup>1</sup> Dongki Jung<sup>1</sup> Christopher Maxey<sup>1,2</sup> Sungmin Eum<sup>2</sup>  
Yonghan Lee<sup>1</sup> Dinesh Manocha<sup>1</sup> Heesung Kwon<sup>2</sup>  
University of Maryland, College Park<sup>1</sup> DEVCOM Army Research Laboratory<sup>2</sup>

## Abstract

Despite significant advancements in dynamic neural rendering, existing methods fail to address the unique challenges posed by UAV-captured scenarios, particularly those involving monocular camera setups, top-down perspective, and multiple small, moving humans, which are not adequately represented in existing datasets. In this work, we introduce UAV4D, a framework for enabling photorealistic rendering for dynamic real-world scenes captured by UAVs. Specifically, we address the challenge of reconstructing dynamic scenes with multiple moving pedestrians from monocular video data without the need for additional sensors. We use a combination of a 3D foundation model and a human mesh reconstruction model to reconstruct both the scene background and humans. We propose a novel approach to resolve the scene scale ambiguity and place both humans and the scene in world coordinates by identifying human-scene contact points. Additionally, we exploit the SMPL model and background mesh to initialize Gaussian splats, enabling holistic scene rendering. We evaluated our method on three complex UAV-captured datasets: VisDrone, Manipal-UAV, and Okutama-Action, each with distinct characteristics and 10 – 50 humans. Our results demonstrate the benefits of our approach over existing methods in novel view synthesis, achieving a 1.5 dB PSNR improvement and superior visual sharpness.

## 1 Introduction

Unmanned Aerial Vehicles (UAVs) have become essential tools for capturing large-scale environments such as streets and urban areas, supporting applications like world mapping, human activity analysis, and security monitoring. Recent advances in neural rendering [40, 26] have enabled photorealistic scene reconstructions from UAV data, driving progress in large-scale mapping. However, most of the existing works [51, 32, 34, 38, 39] primarily focus on static scenes, overlooking the more challenging dynamic scenes, even though real-world environments are inherently dynamic, involving human activities and complex background changes. Although dynamic neural rendering methods are rapidly evolving, most existing approaches [76] focus on phone-captured video scenes [67, 60, 48, 54], multi-view synchronized camera setups [37, 63], or multi-sensor systems scenarios [9] such as multi-camera rigs and LiDAR sensors, as seen in Fig. 1. Despite their relevance, dynamic neural rendering methods tailored for UAV scenarios remain underexplored. To the best of our knowledge, only a few works [38, 39] have attempted this, and they have some limitations. Some approaches use implicit neural representations [15] for volumetric rendering to generate novel-view images but face challenges in terms of maintaining high-fidelity outputs.

Applying dynamic neural rendering to UAV scenes presents two fundamental challenges. First, due to hardware constraints, UAVs typically lack access to a diverse range of sensors and cannot utilize multi-view synchronized camera systems or multi-sensor configurations. Consequently, scene reconstruction must rely solely on monocular dynamic video, which presents substantial



Figure 1: **Comparison between the Existing Benchmarks for Dynamic Neural Rendering and UAV captured Datasets.** UAVs typically cover wide areas from a top-down perspective, capturing dynamic scenes [3, 2, 7] with a distinct setup: they contain numerous human instances (ranging from 10 to 50 per frame), each occupying only a tiny fraction of the image area.

challenges [17] for both accurate geometry reconstruction and photorealistic rendering—particularly in dynamic environments. Furthermore, most dynamic objects in UAV-captured scenes are relatively small and multiple moving humans often appear simultaneously. These conditions pose significant challenges, making it difficult to apply the state-of-the-art approaches [77, 54, 75, 48] that rely on depth estimation [65], optical flow [61] and point tracking models [64, 24, 10]. Even recent 4D reconstruction methods [72, 55, 14] powered by 3D foundation models [56] face difficulties when reconstructing small dynamic humans. This challenge arises primarily because existing large-scale datasets for dynamic scenes rarely include scenarios with small and moving human instances. As a result, many of these previously mentioned methods are ineffective in UAV-based scenarios. Inspired by recent progress in human-scene reconstruction [22, 28], we focus specifically on reconstructing and rendering moving humans, which are a key component of dynamic scenes captured by UAVs.

**Main Results:** We present UAV4D, a novel neural rendering framework that reconstructs dynamic human instances and static backgrounds from UAV-captured real-world data, enabling temporally consistent and photorealistic novel-view synthesis. Our methods begin with reconstructing the joint geometry of small dynamic humans and static backgrounds from monocular UAV videos by integrating SMPL-based human meshes with dense background geometry. We leverage the 3D foundation model [53] to estimate camera poses and perform dense background reconstruction, yielding consistent and robust background meshes across diverse scenarios. We observe that HMR2 [19] and SAM2 [45] exhibit strong performance in UAV contexts, and we adopt them to recover 4D human motion trajectories as temporally aligned SMPL body meshes [35] from monocular videos. However, the human and background meshes suffer from inconsistent scales, and the absolute global positioning of the human meshes remains unknown. To resolve these discrepancies, we propose a scale optimization technique that aligns the background geometry from the 3D foundation model to the metric human mesh, estimating an optimal global scale parameter. Using the optimized scale parameter, we unify the background and human meshes within a consistent world coordinate system over time. Finally, we localize the human mesh in the world space by unprojecting the 2D ground contact point into a 3D location on the reconstructed background mesh.

We then initialize separate 3D Gaussian representations for humans and background using their respective geometric reconstructions. We maintain separate Gaussian splats for humans and background, which are jointly optimized and composited to render photorealistic full frames. Our approach explicitly decomposes dynamic human instances and static backgrounds by independently optimizing their Gaussian splats. By initializing with a strong Gaussian prior from the human SMPL mesh, we ensure that the optimization process properly learns the human Gaussian splats, rather than neglecting them due to their small pixel regions. The key contributions of this work include:

- We introduce UAV4D, the first neural rendering framework that reconstructs dynamic human motions and static backgrounds from UAV-captured monocular videos, enabling temporally consistent and photorealistic novel-view synthesis of full scenes.
- We propose a novel method for resolving the scale ambiguity issue in 3D foundation models and for aligning multiple human meshes with the background mesh. We also present a human placement method by identifying the ground contact point. By initializing both the human and background meshes in world coordinates, we decompose the human and background Gaussian splats to render the complete image.
- To the best of our knowledge, UAV4D is the first to enable dynamic Gaussian splatting for UAV-captured scenes with large number of small moving humans (e.g., up to 50). We evaluated its

performance on three datasets with unique characteristics, our method achieves state-of-the-art rendering quality, outperforming prior methods by up to 1.5 dB in PSNR.

## 2 Related Work

**3D Reconstruction for Static and Dynamic Scenes.** Traditional 3D reconstruction typically consists of two components: Structure-from-Motion (SfM) and Multi-View Stereo (MVS) systems. SfM [59, 46] extracts and matches features across multi-view images to estimate camera poses and sparse 3D points via triangulation [20]. MVS [16, 47] then estimates dense depth maps for each image by performing an accurate and efficient global search for the optimal 3D plane hypotheses. Recently, learning-based SfM [49, 50, 58, 52] and MVS [68, 70, 27, 71, 56, 53] approaches have leveraged large-scale datasets to enable end-to-end differentiable SfM and dense reconstruction. Notably, DUS<sub>t</sub>3R [56] and MAS<sub>t</sub>3R [31, 13] have emerged as breakthroughs by estimating globally consistent point maps from just two views without requiring any camera information. VGGT [53] also leverages point maps during training and modifies the network architecture by incorporating alternative attention mechanisms for improved global alignment. However, these methods are primarily designed for static scenes and struggle to handle dynamic components such as humans. Early methods for non-rigid reconstruction relied on RGB-D sensors [79, 43, 11, 21] for dense tracking and reconstruction, or employed non-rigid SfM approaches [1, 18, 78]. Alternatively, researchers have utilized learning-based methods that leverage large datasets to train neural networks. Some works [74, 23] train monocular depth estimation networks using pre-computed optical flow, or jointly optimize depth and camera poses [29]. More recently, concurrent studies [31, 13, 14, 36] have achieved remarkable ability in dynamic scenes by fine-tuning MAS<sub>t</sub>3R [13] with large-scale dynamic datasets to estimate both camera poses and point maps. However, none of these previous methods perform well on UAV-captured datasets, as the humans in our data are relatively small compared to those in their training datasets. Therefore, we decompose the scene into static and dynamic components, leveraging the prediction results of VGGT for separate tasks within our pipeline.

**Dynamic Neural Rendering.** In the field of neural rendering, Neural Radiance Fields (NeRF) [40] and 3D Gaussian Splatting (3DGS) [26] are milestone works that enable novel view synthesis of static scenes from multi-view images. NeRF-based methods [4, 5, 42, 6] use a multilayer perceptron (MLP) to represent the scene implicitly, while 3DGS [26] employs a set of 3D Gaussian primitives that are differentially splatted onto the 2D image plane. Researchers have increasingly adopted 3DGS for its more efficient rendering performance [8]. Earlier methods were limited to static scenes, but researchers quickly extended them to handle dynamic scenes. One popular direction [67, 60, 48, 33] is deformation field-based methods, which often use a time-conditioned deformation network to warp 3D Gaussians into each time frame. Another line of work [66, 12] directly models 4D Gaussian primitives by integrating 3D Gaussians with the time dimension. Some approaches [77, 54, 75, 48] estimate 3D scene motion and point correspondences using pretrained models [61, 10, 65, 24, 64] to deform 3D Gaussians. HuGS [28] presents an approach similar to ours, using Gaussian splats to represent both humans and the scene. However, as their target scenes consist of phone-captured videos [22], they focus exclusively on a single, large person within the scene. Most of these methods are not designed for UAV-captured datasets, as they struggle to handle scenes with multiple pedestrians (more than 10 people) and very small human figures. UAV-Sim [38] and TK-planes [39] are similar tasks to ours, as they use multi-resolution feature spaces in NeRF to represent small dynamic objects. However, we take a different approach by reconstructing the human and background meshes to initialize the Gaussian splats. We then render all the Gaussian splats to generate the full images.

## 3 Method

Our method takes as input monocular videos of human-centric scenes [2, 7, 3] captured by UAVs. Given this input, our goal is to enable dynamic neural rendering using 3D Gaussian splatting [26]. To achieve this, our approach involves initializing the human-scene from 2D images, reconstructing the 3D geometry of both the human and the scene, and optimizing the Gaussian splats for dynamic neural rendering.

### 3.1 Preliminaries

**3D Gaussian Splatting (3DGS)** [26] represents scenes as an unordered set of 3D Gaussian primitives, rendered through a differentiable rasterization process [80]. Each Gaussian component  $g_i$  is defined as its mean  $\mu_i \in \mathbb{R}^3$  and 3D covariance  $\Sigma_i \in \mathbb{R}^{3 \times 3}$ . The covariance matrix is decomposed into two learnable components, a scaling matrix  $S_i \in \mathbb{R}^3$  and a rotation matrix  $R_i \in \mathbb{R}^{3 \times 3}$ , as  $\Sigma_i =$

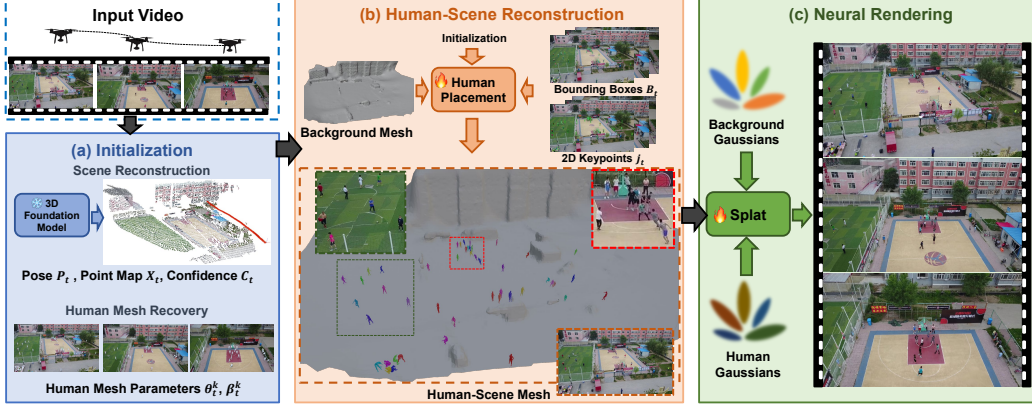


Figure 2: **Overview of Our Approach:** In Section 3.2, we begin the initialization process for reconstructing the background scene and the human mesh. Then, in Section 3.3, we reconstruct the background mesh, determine the optimal scale for alignment, and position the human mesh by identifying the ground contact points. In Section 3.4, we jointly optimize the human and background Gaussians for rendering.

$R_i S_i S_i^T R_i^T$ . Furthermore, each Gaussians store an opacity logit  $o_i \in \mathbb{R}$  and color  $c_i$  defined by spherical harmonics (SH) coefficients. To render an image from a given view, the color of each pixel is computed by  $\alpha$ -blending  $K$  ordered Gaussians using the following equation:  $C = \sum_{i=1}^K c_i \alpha_i \prod_{j=1}^{i-1} (1 - \alpha_j)$  where density  $\alpha_i$  is computed by the multiplication of 2D Gaussians with covariance  $\Sigma'_i \in \mathbb{R}^{2 \times 2}$  and a learnable point-wise opacity  $o_i$ .

**Skinned Multi-Person Linear (SMPL) Model** [35] is a commonly used parametric human body model. The SMPL model exploits a template human mesh in the canonical rest pose, defined as  $\mathcal{M}_h \in (\mathcal{V}_c, \mathcal{F})$  with vertices  $\mathcal{V}_c \in \mathbb{R}^{6890 \times 3}$ . It takes body shape parameters  $\theta, \beta$  as input and outputs a posed 3D mesh with deformed vertices, where  $\theta \in \mathbb{R}^{24 \times 3 \times 3}$  and  $\beta \in \mathbb{R}^{10}$  represent the pose and shape parameters, respectively. The pose parameters  $\theta$  consist of the global rotation of the root joint (pelvis), and the 23 local rotations of other articulated joints relative to their parents along the kinematic chain. SMPL uses  $n_b$  predefined joints and Linear Blend Skinning (LBS) weights  $W$ , defined as  $W(v_c) = \{w_1, \dots, w_{n_b}\}$ . The vertex  $v_c$  in the canonical template mesh can be deformed to the articulated space via the LBS, as  $v = (\sum_{k=1}^{n_b} W_k(v_c) B_k) v_c$ , where  $B = \{B_1, \dots, B_{n_b}\}$  is the target joint transformation.

### 3.2 Initialization

At this stage, we first utilize off-the-shelf models [53, 19, 45] to obtain initial estimates, such as camera poses, point maps, human masks, human meshes, and other relevant data, for reconstructing the geometry of both the background scene and the human.

**Scene.** Given a monocular video sequence  $\{I_t \in \mathbb{R}^{H \times W \times 3}\}_{t=1}^N$ , we first employ a 3D foundation model [53] to estimate camera poses  $\{P_t\}_{t=1}^N$  including intrinsics  $K$  and extrinsics, rotation  $R_t$  and translation  $T_t$ , per-view point map  $X_t \in \mathbb{R}^{H \times W \times 3}$  and corresponding confidence  $C_t \in \mathbb{R}^{H \times W \times 1}$ .

**Human.** Due to the relatively small size of the human subjects, it is challenging to apply recent 3D tracking systems [19] trained on standard tracking tasks. Since our goal is precise reconstruction and rendering, we use bounding boxes  $\{B_t^k\}_{k=1}^{K_t}$  as prompts for SAM2 [45] to generate accurate instance masks for  $K_t$  humans. These human segmentation masks  $\{M_t^k\}_{k=1}^{K_t}$  are then fed into HMR2.0 [19] to predict camera-frame human meshes from each image  $I_t$  for  $K_t$  detected people. Thus, we can obtain the human mesh parameters for each human, defined as  $\{\theta_t^k, \beta_t^k\}_{k=1}^{K_t}$  at timestep  $t$ .

**Human Mesh Refinement.** However, due to the challenging nature of UAV imagery, HMR2.0 [19] often produces noisy initializations. We introduce a refinement method to remove human mesh parameters with poor quality. Since the human meshes reside in the camera coordinate system, we project each individual human mesh into the image space and compute the bounding box  $\{\bar{B}_t^k\}_{k=1}^{K_t}$  for each projected human. We then calculate the ratio between  $B_t^k$  and  $\bar{B}_t^k$ , and remove any human meshes for which  $\bar{B}_t^k / B_t^k$  exceeds a threshold  $\eta_{box}$ . Furthermore, we measure the overlap between dilated human masks  $M_{t-1}^k, M_{t+1}^k$  from the previous and next time frames. If the current bounding box with missing human mesh parameters overlaps in both adjacent frames, we interpolate the



missing parameters  $\theta_t^k, \beta_t^k$  using the human mesh parameters from the previous frame ( $\theta_{t-1}^k, \beta_{t-1}^k$ ) and the next frame ( $\theta_{t+1}^k, \beta_{t+1}^k$ ) applying linear interpolation to both the quaternion pose parameters and the shape vectors.

### 3.3 Joint Human-Scene Reconstruction

Although our initialization provides a reasonable estimate of human poses, all predictions remain in the camera coordinate space. As a result, when the camera moves, the estimated human motion becomes implausible. To align the human and scene in the world coordinate, we reconstruct the background region and identify human-ground contact points to position the human mesh in the scene accurately. We observe that UAVs typically capture wide-area footage with the full human body visible, allowing us to leverage 2D bounding boxes to estimate the human-ground contact points. However, aligning the human mesh with the background remains challenging due to two key issues: (1) in complex environments, the reconstructed background geometry is often noisy and structurally intricate, making it difficult to reliably detect human-scene contact points; and (2) the inherent scale ambiguity of the 3D foundation model [53].

**Background Geometry Reconstruction.** To address the first issue, we first utilize all point maps  $\{X_t\}_{t=1}^N$  and corresponding confidence map  $\{C_t\}_{t=1}^N$  for background reconstruction. The point map represents a dense, pixel-aligned 3D location map for each corresponding image in the world coordinate frame. We stack all these point maps to represent the 3D geometry of the entire scene, although they include noisy points. Then, we compute the  $\eta_{conf}$  percentile of the pixel-aligned confidence values and use it to filter the point maps, removing noisy dynamic regions and intricate geometries with low confidence. The filtered point maps are then stacked, and Poisson surface reconstruction [25] is applied to generate the background mesh  $\mathcal{M}_{bg}$ . Thanks to this filtering, the background mesh is generated as a clean, flat ground surface, free from noisy dynamic human regions or complex structures that would otherwise make it difficult to identify human-scene contact points.

**Scale Optimization.** Furthermore, to address the scale ambiguity issue of the 3D foundation model [53], we propose an alignment method between the background and the human mesh. Since the human mesh generated by SMPL [35] is defined in metric scale, we can align the background mesh relative to the metric human mesh. We introduce a scale parameter,  $\sigma$ , which adjusts the point maps  $X_t$ , background mesh  $\mathcal{M}_{bg}$ , and camera poses accordingly.

Our idea is to optimize the scale parameter from a *bone length* perspective. Inspired by [41], we leverage the correlation between observed 2D keypoints and 3D joints for this alignment. We first use ViTPose [62] to detect 2D keypoints  $j^k$  for each person  $k$  in the image. Then, we lift the 2D keypoints  $j_t^k$  to 3D joints using scaled point maps  $X_t$ , defined as  $\hat{J}_t^k = \sigma X_t(i, j)$  where  $(i, j) \in j_t^k$ . Given the human mesh parameters  $\theta_t^k, \beta_t^k$  from HMR2.0 [19], we can obtain the 3D location  $J_i$  of interest joint  $i$  from the mesh. Then we compute the 3D bone length  $d_{(p,c)}^k$  for each joint pair  $(p, c)$  associated with the main body joints  $\mathcal{J}_{body}$  of person  $k$  in the image at time  $t$ , as defined by:

$$\hat{d}_{(p,c),t}^k = J_p(\theta_t^k, \beta_t^k) - J_c(\theta_t^k, \beta_t^k) \quad \text{and} \quad d_{(p,c),t}^k(\sigma) = \sigma X_t(p) - \sigma X_t(c). \quad (1)$$

The loss function  $L(\sigma)$  is computed as the L2 norm loss between the predicted 3D joint-based bone lengths  $\hat{d}_{(p,c),t}^k$  and the corresponding ground-truth values  $d_{(p,c),t}^k(\sigma)$ . Specifically, the loss is calculated across all time steps  $t$ , individuals  $k$ , and joints  $(p, c)$  in the main body, where minimizing this loss ensures that the predicted bone lengths align closely with the ground truth. The scale parameter  $\sigma$  is optimized using the L-BFGS algorithm [44] applied to this loss. The loss function for optimizing the scale parameter  $\sigma$  is as follows:

$$L(\sigma) = \sum_t \sum_{k \in \mathcal{K}} \sum_{(p,c) \in \mathcal{J}_{body}} \|\hat{d}_{(p,c),t}^k - d_{(p,c),t}^k(\sigma)\|_2. \quad (2)$$

The update rule is  $\sigma_{n+1} = \sigma_n - \alpha \mathcal{H}_n \nabla L(\sigma_n)$  where  $\alpha$  is the learning rate and,  $\mathcal{H}_n$  is the approximation of the inverse Hessian. The optimization proceeds for  $T_{opt}$  steps, and the objective is minimized through gradient-based optimization.

**Human Placement.** After determining the optimal scale  $\sigma$ , we apply this scale to the background mesh  $\mathcal{M}_{bg}$  and camera poses  $P_t$  to align them with the human mesh. In conjunction with the camera pose, it is necessary to initialize the root translation in the world coordinate system. Our approach takes advantage of the fact that UAV-captured images provide top-down views, which facilitate the identification of the ground contact point. This contact point serves as a plausible initial estimate for the root translation. Given the background mesh  $\mathcal{M}_{bg}$ , we render the depth map  $D_t$  from the

specified viewpoint. Using the 2D bounding box  $B_t^k = (x_{\min}, y_{\min}, x_{\max}, y_{\max})$  projected from the human mesh, we detect the 2D contact point as  $(x_c, y_c) = ((x_{\min} + x_{\max})/2, y_{\max})$ . Subsequently, we use the depth value from  $D_t$  to unproject this 2D contact point for each individual human into the world coordinate system as follows:

$$\psi_t = \sigma R^T [K^{-1} D_{x_c, y_c} [x_c, y_c, 1]^T] - \sigma R^T T. \quad (3)$$

$\psi_t$  is the 3D ground contact point in the world coordinate.

With this information, we can accurately position all individual human meshes within the background mesh, with all meshes defined in the world coordinate system, as seen in Fig. 3.

### 3.4 3D Gaussian Scene Modeling

We model the scene using distinct Gaussian representations for dynamic humans and the static background, ensuring both temporal coherence and rendering clarity. We employ standard 3D Gaussians to model the background Gaussians  $g_{bg}$  and the human Gaussians  $g_h$ . Following Sec. 3.1, both Gaussians  $g_h$  and  $g_{bg}$  contain learnable attributes  $(\mu, r, s, c, o)$ , which represent the 3D mean, 3D rotation, scaling factor, opacity factor, and color value, respectively. These are then merged into a unified human-scene primitive  $g_{all} = g_{bg} + g_h$ , which is subsequently fed into the Gaussian rasterizer [26] for rendering.

**Background Gaussians.** The background is represented by static Gaussians  $g_{bg}$ , which are initialized using stacked multi-view point maps  $X_t$ . For UAV scenes captured at high altitudes, we use all point maps without filtering. In contrast, for UAV scenes captured at low altitudes, we employ a confidence map to filter the point maps and use human masks  $M_t^k$  to remove point maps corresponding to human regions, stacking only the static background regions.

**Human Gaussians.** For human Gaussians, inspired by GART [30], we utilize the canonical template mesh  $\mathcal{M}_h$  in the rest pose to represent the 3D Gaussian splats. The skinning transformation for each Gaussian,  $A(t) = (R_A(t), T_A(t))$ , is derived from the LBS weight  $LBS(g_h, \theta_t)$ , which transform the canonical Gaussian positions  $\mu$  and rotations  $r$  to the world frame.

$$g_h(t) = (R_A(t)\mu + T_A(t) + \psi_t, R_A(t) \cdot r, s, c, o). \quad (4)$$

The changes in  $\theta_t$  over time result in updates to the transformations of the key joints and linearly interpolates Gaussians to obtain the deformed position  $\mu(t)$  and rotations  $r(t)$  at different time steps.

**Optimization.** We optimize all Gaussian attributes  $g_{bg}, g_h$ , the human poses of all SMPL parameters  $\theta_t, \psi_t$  for each frame  $t$  and the corresponding skinning weights.

The overall loss function for optimization is defined as:

$$L_{total} = (1 - \lambda_{pho})L_1 + \lambda_{pho}L_{ssim} + \lambda_o L_o + L_{smpl}, \quad (5)$$

where  $L_1$  and  $L_{ssim}$  represent the photometric loss between the rendered full image and the ground truth image.  $L_{smpl}$  consists of various loss terms related to human Gaussian splats and human regions. Details are provided in the supplementary material.

## 4 Experimental Results

To measure the effectiveness of UAV4D, we evaluate our method on novel view synthesis tasks, using every 8th frame as the held-out test set. We report PSNR, SSIM [57], and LPIPS [73] for full images and human-related regions, to assess dynamic reconstruction capabilities. The human regions are obtained using a pretrained segmentation model which get a prompt from groundtruth bonding box.

### 4.1 Datasets and Baselines

**VisDrone:** The VisDrone dataset [7] is a standard benchmark for object detection and tracking in the UAV research community. It was captured at altitudes of 40 to 50 meters in China under varying weather and illumination conditions. This dataset includes many densely packed small objects in

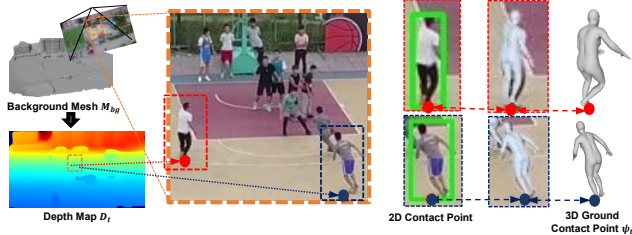


Figure 3: **Human Placement.** We identify the 2D contact point from the bounding box and use the depth from the mesh to unproject the 3D ground contact point.

Table 1: **Quantitative Comparison** of our method with recent comparative works on the three datasets. Our method achieves the best performance across every category except for PSNR on the Manipal-UAV dataset. Please see the Appendix for detailed comparisons on the four scenes in each dataset. Red, orange, and yellow indicate the first, second, and third best performing algorithms for each metric, respectively.

Method	Okutama-Action			Manipal-UAV			VisDrone		
	PSNR $\uparrow$	SSIM $\uparrow$	LPIPS $\downarrow$	PSNR $\uparrow$	SSIM $\uparrow$	LPIPS $\downarrow$	PSNR $\uparrow$	SSIM $\uparrow$	LPIPS $\downarrow$
TK-Planes [39]	28.05	0.796	0.417	27.98	0.718	0.396	23.98	0.644	0.450
3DGS [26]	29.90	0.867	0.228	29.46	0.856	0.150	24.59	0.782	0.220
4DGS [60]	25.90	0.780	0.410	30.87	0.843	0.253	22.58	0.628	0.440
DeformableGS [67]	22.64	0.748	0.443	31.22	0.894	0.114	15.46	0.522	0.614
UAV4D (Ours)	30.36	0.875	0.184	30.94	0.897	0.084	26.03	0.800	0.147

Table 2: **Quantitative Comparison** of our method with recent comparative works is conducted on the three datasets, focusing on **human-only** regions cropped using precise human masks. Due to the small size of the human regions, it is not possible to compute the LPIPS metric. Consequently, we report only the PSNR and SSIM metrics. Please see the Appendix for detailed comparisons on the four scenes in each dataset. Red, orange, and yellow indicate the first, second, and third best performing algorithms for each metric, respectively.

Method	Okutama-Action		Manipal-UAV		VisDrone	
	PSNR $\uparrow$	SSIM $\uparrow$	PSNR $\uparrow$	SSIM $\uparrow$	PSNR $\uparrow$	SSIM $\uparrow$
TK-Planes [39]	19.14	0.631	18.38	0.752	17.65	0.544
3DGS [26]	19.07	0.656	17.99	0.748	16.51	0.548
4DGS [60]	18.18	0.602	19.23	0.770	16.25	0.510
DeformableGS [67]	16.33	0.571	18.65	0.762	12.59	0.354
UAV4D (Ours)	19.49	0.664	19.38	0.784	17.98	0.604

UAV images. We selected four different scenes that primarily consist of pedestrians and complex background environments.

**Okutama-Action:** The Okutama-Action dataset [3] contains video sequences of 12 action categories, captured using cameras mounted on two flying UAVs at altitudes ranging from 10 to 45 meters. We chose four scenes that exhibit significant camera variation and distinct viewing angles.

**Manipal-UAV:** The Manipal-UAV dataset [2] is designed for person detection in UAV images. It was acquired in India using two UAVs flying at altitudes between 10 and 50 meters. Unlike the previous datasets, it explicitly provides altitude information. We selected four scenes captured at 40 and 50 meters, representing the highest-altitude cases.

**Baselines:** To evaluate rendering quality, we compare our method with four comparative methods: TK-Planes [39], 3DGS [26], Deformable-3DGS [67], and 4DGS [60]. To the best of our knowledge, TK-Planes [39] is the only work that has specifically designed dynamic NeRFs for UAV scenes, while 4DGS [60] and Deformable-3DGS [67] represent the state-of-the-art methods in dynamic Gaussian-splatting.

## 4.2 Quantitative Comparison

In Table 1, we present the rendering quality of novel-view synthesis across three datasets. We compute the average rendering metrics across 4 scenes for VisDrone [7], 4 scenes for Manipal-UAV [2], and 4 scenes for Okutama-Action [3]. Due to the small size of the human subjects in UAV datasets, the rendering metrics for the full image do not reflect the dynamic rendering quality of the human regions directly. Moreover, since the Manipal-UAV dataset was captured at an exceptionally high altitude, the rendering metrics of the full image are less informative regarding the human regions and instead provide a better indication of the background region’s rendering quality. In contrast, the VisDrone dataset contains multiple humans, with relatively larger pixel regions compared to other datasets, allowing the full image rendering quality to be more directly correlated with the holistic scene rendering quality. Furthermore, certain scenes in VisDrone feature a significant number of moving pedestrians (approximately 30–50 individuals), presenting a particularly challenging scenario for dynamic reconstruction. Our method demonstrates superior rendering quality compared to other recent approaches, underscoring its robustness. In the Okutama-Action dataset, our method also exhibits better rendering quality than alternative methods. The Okutama-Action dataset is characterized by substantial camera variation and distinct viewing angles, which can destabilize deformation-field-based methods. However, our method shows strong resilience in handling these dynamic scenes, which involve substantial pose variation and changes in viewing angle.

In the VisDrone and Okutama-Action datasets, we observe that the training of 4DGS [60] and Deformable-GS [67] is unstable, with the training of deformation-based fields often failing. We attribute this instability to the presence of multiple small moving objects within the scenes, which



Figure 4: **Quantitative Comparison of VisDrone Dataset [7]**. We visualize the zoomed-in blue and red regions, which emphasize the dynamic humans. Our method demonstrates superior capability in reconstructing small, moving humans compared to other existing approaches.

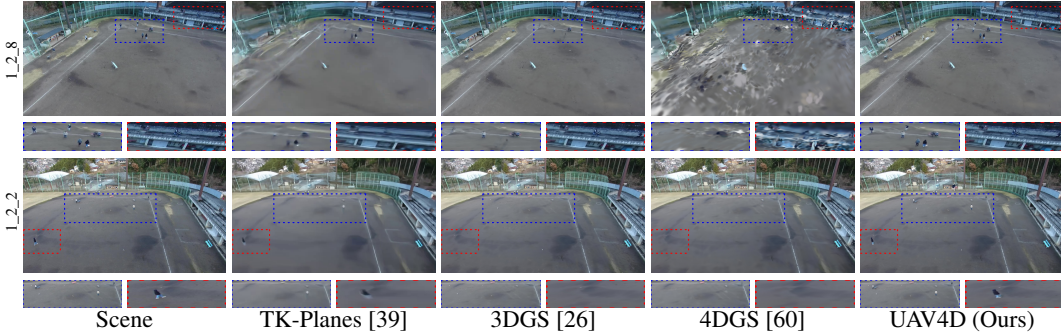


Figure 5: **Quantitative Comparison of Okutama-Action Dataset [3]**. We visualize the zoomed-in blue and red regions, which emphasize the dynamic humans. Our method demonstrates superior capability in reconstructing small, moving humans compared to other existing approaches.

indicates that a single deformation field is insufficient to capture the required deformations accurately. As a result, the training process for these models becomes highly unstable. In contrast, TK-planes [39] demonstrates greater robustness across various dynamic scenes, yielding superior performance. For the Manipal-UAV dataset, our method outperforms others in most cases, except for the PSNR values for Deformable-GS [67]. We observe that Deformable-GS [67] delivers superior rendering performance in regions with dense foliage and moving vegetation (e.g., swaying leaves). Our method currently struggles to represent such deformations, particularly in swaying trees, which cover large areas in UAV-captured datasets.

Table 2 reports the rendering quality across three datasets, focusing on human-only regions cropped using precise human masks. Due to the small pixel size of the human regions, we are unable to use the LPIPS [73] metric, which relies on pretrained neural networks to measure metrics. Across all datasets, our method demonstrates superior rendering quality for human regions compared to other approaches. This indicates that our strategy effectively reconstructs and renders dynamic humans.

**Ablation Study** Table 3 presents the results of an ablation study, averaged across four scenes in the Visdeon dataset. “Ours wo SMPL” indicates the version where we did not use human Gaussian splats, thus reconstructing only the background splats, which limits the model to static humans and removes moving people. “Ours wo Scale” refers to the version where the human mesh is placed without scale optimization. In this case, we set the initial scale  $\sigma$  to 40 and place the human mesh without any scale adjustment, leading to misalignment between the human regions and the human mesh. “Ours wo Refine” follows the full pipeline but omits the human mesh refinement process described in Sec. 3.2. This version shows a slight improvement in artifacts caused by inaccurate in the human mesh.

Table 3: **Ablation Study** on VisDrone Dataset. Please see the Appendix for details.

Method	PSNR $\uparrow$	SSIM $\uparrow$	LPIPS $\downarrow$
Ours	26.03	0.800	0.147
Ours wo SMPL	24.33	0.763	0.212
Ours wo Scale	23.02	0.651	0.25
Ours wo Refine	25.79	0.772	0.165



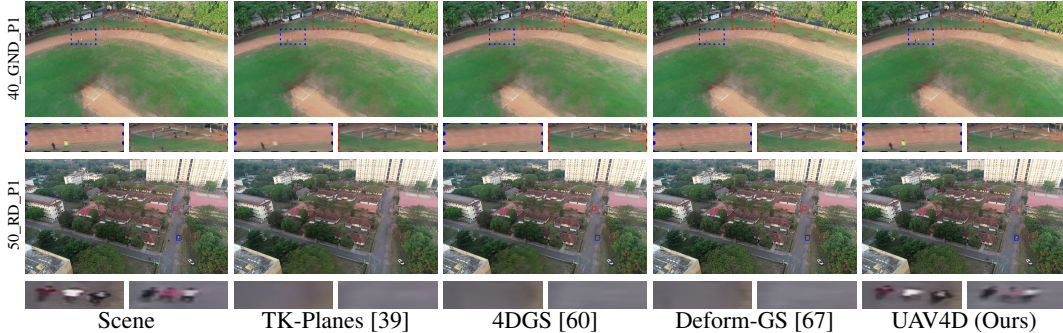


Figure 6: **Quantitative Comparison of Manipal-UAV Dataset [2]**. We visualize the zoomed-in blue and red regions, which emphasize the dynamic humans. Our method demonstrates superior capability in reconstructing small, moving humans compared to other existing approaches. The rendering results of 3DGS [26] are not included, as this method ignores moving humans, similar to other methods.

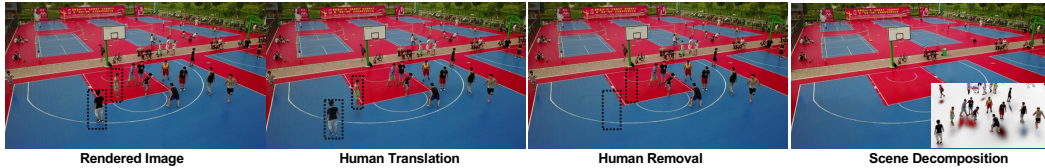


Figure 7: **Scene Editing Samples**: Due to the nature of scene decomposition, we can move or remove the humans within the black-dotted boxes. The fourth image illustrates the decomposition of the background and humans. For additional visual results, please refer to the supplementary materials.

### 4.3 Qualitative Comparison

Figure 4 presents visual examples from the VisDrone dataset [7]. Overall, our method achieves the highest rendering quality, producing a photorealistic background and sharp human regions, where the detailed shapes of the humans are more accurately recovered compared to other methods. TK-planes [39] generates blurred renderings, while 3DGS [26] is unable to represent moving individuals, although it successfully reconstructs clear background regions. The training of 4DGS [60] occasionally fails. A similar trend is observed in the Okutama-Action dataset [3], as shown in Figure 5. Figure 6 displays examples from the Manipal-UAV dataset [2]. Our method can reconstructs extremely small humans, occupying only around  $10 \times 10$  pixels, outperforming all other methods. However, Deformable-GS [67] shows better performance in rendering swaying leaves and trees, which are frequently observed in this dataset.

**Scene Editing** Since our Gaussian scene is composed of separate human and background Gaussians, our system enables scene editing. As demonstrated in Fig. 7, we can easily remove, and translate humans, thanks to the decomposition of the foreground and background. This capability can be extended to downstream applications, such as simulating dynamic scenes captured by UAV that are expensive to capture in the real world.

## 5 Conclusion, Limitations, and Future Work

We have introduced UAV4D, a method for dynamic Gaussian splatting in UAV-captured environments. We propose a scale optimization and human placement technique to reconstruct human-scene geometry in the world coordinate system. This human-scene geometry is then used to initialize 3D Gaussian splats for dynamic scenes. It is important to note that the explicit representation of human geometry in our method is crucial for accurately modeling small, moving humans, ensuring they are not neglected during the optimization of Gaussian splats. Our joint optimization approach demonstrates improved performance in novel view synthesis, both for background and human regions. However, our method has several limitations. First, it relies on pretrained models (e.g. HMR2.0 [19] or SAM2 [45]). In particular, HMR2.0 [19] still exhibits inaccuracies in human mesh parameters, which leads to rendering artifacts in the scene. Additionally, other dynamic components, such as bicycles or swaying trees, are not effectively rendered using static background Gaussian splats, except for the human regions. In future work, we plan to modify our human mesh refinement algorithm to better align with 2D images and incorporate segmentation information to represent other dynamic components using dynamic Gaussian splats. Our approach can be combined with downstream UAV applications such as person detection [38] and human action recognition [3].



## References

- [1] Ijaz Akhter, Yaser Sheikh, Sohaib Khan, and Takeo Kanade. Trajectory space: A dual representation for nonrigid structure from motion. *IEEE Transactions on Pattern Analysis and Machine Intelligence*, 33(7): 1442–1456, 2010.
- [2] KR Akshatha, AK Karunakar, B Satish Shenoy, K Phani Pavan, V Dhareshwar Chinmay, et al. Manipal-uav person detection dataset: A step towards benchmarking dataset and algorithms for small object detection. *ISPRS Journal of Photogrammetry and Remote Sensing*, 195:77–89, 2023.
- [3] Mohammadamin Barekatin, Miquel Martí, Hsueh-Fu Shih, Samuel Murray, Kotaro Nakayama, Yutaka Matsuo, and Helmut Prendinger. Okutama-action: An aerial view video dataset for concurrent human action detection. In *Proceedings of the IEEE conference on computer vision and pattern recognition workshops*, pages 28–35, 2017.
- [4] Jonathan T Barron, Ben Mildenhall, Matthew Tancik, Peter Hedman, Ricardo Martin-Brualla, and Pratul P Srinivasan. Mip-nerf: A multiscale representation for anti-aliasing neural radiance fields. In *Proceedings of the IEEE/CVF International Conference on Computer Vision*, pages 5855–5864, 2021.
- [5] Jonathan T Barron, Ben Mildenhall, Dor Verbin, Pratul P Srinivasan, and Peter Hedman. Mip-nerf 360: Unbounded anti-aliased neural radiance fields. In *Proceedings of the IEEE/CVF Conference on Computer Vision and Pattern Recognition*, pages 5470–5479, 2022.
- [6] Jonathan T Barron, Ben Mildenhall, Dor Verbin, Pratul P Srinivasan, and Peter Hedman. Zip-nerf: Anti-aliased grid-based neural radiance fields. In *Proceedings of the IEEE/CVF International Conference on Computer Vision*, pages 19697–19705, 2023.
- [7] Yaru Cao, Zhijian He, Lujia Wang, Wenguan Wang, Yixuan Yuan, Dingwen Zhang, Jinglin Zhang, Pengfei Zhu, Luc Van Gool, Junwei Han, et al. Visdrone-det2021: The vision meets drone object detection challenge results. In *Proceedings of the IEEE/CVF International conference on computer vision*, pages 2847–2854, 2021.
- [8] Adam Celarek, George Kopanas, George Drettakis, Michael Wimmer, and Bernhard Kerbl. Does 3d gaussian splatting need accurate volumetric rendering? In *Computer Graphics Forum*, page e70032. Wiley Online Library, 2025.
- [9] Ziyu Chen, Jiawei Yang, Jiahui Huang, Riccardo de Lutio, Janick Martinez Esturo, Boris Ivanovic, Or Litany, Zan Gojcic, Sanja Fidler, Marco Pavone, Li Song, and Yue Wang. Omnire: Omni urban scene reconstruction. In *The Thirteenth International Conference on Learning Representations*, 2025.
- [10] Carl Doersch, Yi Yang, Mel Vecerik, Dilara Gokay, Ankush Gupta, Yusuf Aytar, Joao Carreira, and Andrew Zisserman. Tapir: Tracking any point with per-frame initialization and temporal refinement. In *Proceedings of the IEEE/CVF International Conference on Computer Vision*, pages 10061–10072, 2023.
- [11] Mingsong Dou, Sameh Khamis, Yury Degtyarev, Philip Davidson, Sean Ryan Fanello, Adarsh Kowdle, Sergio Orts Escolano, Christoph Rhemann, David Kim, Jonathan Taylor, et al. Fusion4d: Real-time performance capture of challenging scenes. *ACM Transactions on Graphics (ToG)*, 35(4):1–13, 2016.
- [12] Yuanxing Duan, Fangyin Wei, Qiyu Dai, Yuhang He, Wenzheng Chen, and Baoquan Chen. 4d-rotor gaussian splatting: towards efficient novel view synthesis for dynamic scenes. In *ACM SIGGRAPH 2024 Conference Papers*, pages 1–11, 2024.
- [13] Bardienus Duisterhof, Lojze Zust, Philippe Weinzaepfel, Vincent Leroy, Yohann Cabon, and Jerome Revaud. Mast3r-sfm: a fully-integrated solution for unconstrained structure-from-motion. *arXiv preprint arXiv:2409.19152*, 2024.
- [14] Haiwen Feng, Junyi Zhang, Qianqian Wang, Yufei Ye, Pengcheng Yu, Michael J Black, Trevor Darrell, and Angjoo Kanazawa. St4rtrack: Simultaneous 4d reconstruction and tracking in the world. *arXiv preprint arXiv:2504.13152*, 2025.
- [15] Sara Fridovich-Keil, Giacomo Meanti, Frederik Rahbæk Warburg, Benjamin Recht, and Angjoo Kanazawa. K-planes: Explicit radiance fields in space, time, and appearance. In *Proceedings of the IEEE/CVF Conference on Computer Vision and Pattern Recognition*, pages 12479–12488, 2023.
- [16] Yasutaka Furukawa and Carlos Hernández. Multi-view stereo: A tutorial. *Foundations and Trends® in Computer Graphics and Vision*, 9(1-2):1–148, 2015.

- [17] Hang Gao, Ruilong Li, Shubham Tulsiani, Bryan Russell, and Angjoo Kanazawa. Monocular dynamic view synthesis: A reality check. Advances in Neural Information Processing Systems, 35:33768–33780, 2022.
- [18] Ravi Garg, Anastasios Roussos, and Lourdes Agapito. Dense variational reconstruction of non-rigid surfaces from monocular video. In Proceedings of the IEEE Conference on computer vision and pattern recognition, pages 1272–1279, 2013.
- [19] Shubham Goel, Georgios Pavlakos, Jathushan Rajasegaran, Angjoo Kanazawa, and Jitendra Malik. Humans in 4d: Reconstructing and tracking humans with transformers. In Proceedings of the IEEE/CVF International Conference on Computer Vision, pages 14783–14794, 2023.
- [20] Richard Hartley and Andrew Zisserman. Multiple view geometry in computer vision. Cambridge university press, 2003.
- [21] Matthias Innmann, Michael Zollhöfer, Matthias Nießner, Christian Theobalt, and Marc Stamminger. Volumedeform: Real-time volumetric non-rigid reconstruction. In Computer Vision—ECCV 2016: 14th European Conference, Amsterdam, The Netherlands, October 11-14, 2016, Proceedings, Part VIII 14, pages 362–379. Springer, 2016.
- [22] Wei Jiang, Kwang Moo Yi, Golnoosh Samei, Oncel Tuzel, and Anurag Ranjan. Neuman: Neural human radiance field from a single video. In European Conference on Computer Vision, pages 402–418. Springer, 2022.
- [23] Dongki Jung, Jaehoon Choi, Yonghan Lee, Deokhwa Kim, Changick Kim, Dinesh Manocha, and Donghwan Lee. Dnd: Dense depth estimation in crowded dynamic indoor scenes. In Proceedings of the IEEE/CVF International Conference on Computer Vision, pages 12797–12807, 2021.
- [24] Nikita Karaev, Ignacio Rocco, Benjamin Graham, Natalia Neverova, Andrea Vedaldi, and Christian Rupprecht. Cotracker: It is better to track together. In European Conference on Computer Vision, pages 18–35. Springer, 2024.
- [25] Michael Kazhdan, Matthew Bolitho, and Hugues Hoppe. Poisson surface reconstruction. In Proceedings of the fourth Eurographics symposium on Geometry processing, volume 7, 2006.
- [26] Bernhard Kerbl, Georgios Kopanas, Thomas Leimkühler, and George Drettakis. 3d gaussian splatting for real-time radiance field rendering. ACM Transactions on Graphics, 42(4), 2023.
- [27] Taekyung Kim, Jaehoon Choi, Seokeon Choi, Dongki Jung, and Changick Kim. Just a few points are all you need for multi-view stereo: A novel semi-supervised learning method for multi-view stereo. In Proceedings of the IEEE/CVF international conference on computer vision, pages 6178–6186, 2021.
- [28] Muhammed Kocabas, Jen-Hao Rick Chang, James Gabriel, Oncel Tuzel, and Anurag Ranjan. Hugs: Human gaussian splats. In Proceedings of the IEEE/CVF conference on computer vision and pattern recognition, pages 505–515, 2024.
- [29] Johannes Kopf, Xuejian Rong, and Jia-Bin Huang. Robust consistent video depth estimation. In Proceedings of the IEEE/CVF Conference on Computer Vision and Pattern Recognition, pages 1611–1621, 2021.
- [30] Jiahui Lei, Yufu Wang, Georgios Pavlakos, Lingjie Liu, and Kostas Daniilidis. Gart: Gaussian articulated template models. In Proceedings of the IEEE/CVF conference on computer vision and pattern recognition, pages 19876–19887, 2024.
- [31] Vincent Leroy, Yohann Cabon, and Jérôme Revaud. Grounding image matching in 3d with mast3r. In European Conference on Computer Vision, pages 71–91. Springer, 2024.
- [32] Jiaqi Lin, Zhihao Li, Xiao Tang, Jianzhuang Liu, Shiyong Liu, Jiayue Liu, Yangdi Lu, Xiaofei Wu, Songcen Xu, Youliang Yan, et al. Vastgaussian: Vast 3d gaussians for large scene reconstruction. In Proceedings of the IEEE/CVF Conference on Computer Vision and Pattern Recognition, pages 5166–5175, 2024.
- [33] Youtian Lin, Zuozhuo Dai, Siyu Zhu, and Yao Yao. Gaussian-flow: 4d reconstruction with dynamic 3d gaussian particle. In Proceedings of the IEEE/CVF Conference on Computer Vision and Pattern Recognition, pages 21136–21145, 2024.
- [34] Yang Liu, Chuanchen Luo, Lue Fan, Naiyan Wang, Junran Peng, and Zhaoxiang Zhang. Citygaussian: Real-time high-quality large-scale scene rendering with gaussians. In European Conference on Computer Vision, pages 265–282. Springer, 2024.

- [35] Matthew Loper, Naureen Mahmood, Javier Romero, Gerard Pons-Moll, and Michael J Black. Smpl: A skinned multi-person linear model. In Seminal Graphics Papers: Pushing the Boundaries, Volume 2, pages 851–866. 2023.
- [36] Jiahao Lu, Tianyu Huang, Peng Li, Zhiyang Dou, Cheng Lin, Zhiming Cui, Zhen Dong, Sai-Kit Yeung, Wenping Wang, and Yuan Liu. Align3r: Aligned monocular depth estimation for dynamic videos. arXiv preprint arXiv:2412.03079, 2024.
- [37] Jonathon Luiten, Georgios Kopanas, Bastian Leibe, and Deva Ramanan. Dynamic 3d gaussians: Tracking by persistent dynamic view synthesis. In 2024 International Conference on 3D Vision (3DV), pages 800–809. IEEE, 2024.
- [38] Christopher Maxey, Jaehoon Choi, Hyungtae Lee, Dinesh Manocha, and Heesung Kwon. Uav-sim: Nerf-based synthetic data generation for uav-based perception. In 2024 IEEE International Conference on Robotics and Automation (ICRA), pages 5323–5329. IEEE, 2024.
- [39] Christopher Maxey, Jaehoon Choi, Yonghan Lee, Hyungtae Lee, Dinesh Manocha, and Heesung Kwon. Tk-planes: Tiered k-planes with high dimensional feature vectors for dynamic uav-based scenes. arXiv preprint arXiv:2405.02762, 2024.
- [40] Ben Mildenhall, Pratul P Srinivasan, Matthew Tancik, Jonathan T Barron, Ravi Ramamoorthi, and Ren Ng. Nerf: Representing scenes as neural radiance fields for view synthesis. Communications of the ACM, 65(1):99–106, 2021.
- [41] Lea Müller, Hongsuk Choi, Anthony Zhang, Brent Yi, Jitendra Malik, and Angjoo Kanazawa. Reconstructing people, places, and cameras. arXiv preprint arXiv:2412.17806, 2024.
- [42] Thomas Müller, Alex Evans, Christoph Schied, and Alexander Keller. Instant neural graphics primitives with a multiresolution hash encoding. arXiv preprint arXiv:2201.05989, 2022.
- [43] Richard A Newcombe, Dieter Fox, and Steven M Seitz. Dynamicfusion: Reconstruction and tracking of non-rigid scenes in real-time. In Proceedings of the IEEE conference on computer vision and pattern recognition, pages 343–352, 2015.
- [44] Jorge Nocedal. Updating quasi-newton matrices with limited storage. Mathematics of computation, 35(151):773–782, 1980.
- [45] Nikhila Ravi, Valentin Gabeur, Yuan-Ting Hu, Ronghang Hu, Chaitanya Ryali, Tengyu Ma, Haitham Khedr, Roman Rädle, Chloe Rolland, Laura Gustafson, et al. Sam 2: Segment anything in images and videos. arXiv preprint arXiv:2408.00714, 2024.
- [46] Johannes L Schonberger and Jan-Michael Frahm. Structure-from-motion revisited. In Proceedings of the IEEE Conference on Computer Vision and Pattern Recognition, pages 4104–4113, 2016.
- [47] Johannes L Schönberger, Enliang Zheng, Jan-Michael Frahm, and Marc Pollefeys. Pixelwise view selection for unstructured multi-view stereo. In European Conference on Computer Vision, pages 501–518. Springer, 2016.
- [48] Colton Stearns, Adam Harley, Mikaela Uy, Florian Dubost, Federico Tombari, Gordon Wetzstein, and Leonidas Guibas. Dynamic gaussian marbles for novel view synthesis of casual monocular videos. In SIGGRAPH Asia 2024 Conference Papers, pages 1–11, 2024.
- [49] Zachary Teed and Jia Deng. Deepv2d: Video to depth with differentiable structure from motion. arXiv preprint arXiv:1812.04605, 2018.
- [50] Zachary Teed and Jia Deng. Droid-slam: Deep visual slam for monocular, stereo, and rgb-d cameras. Advances in neural information processing systems, 34:16558–16569, 2021.
- [51] Haithem Turki, Deva Ramanan, and Mahadev Satyanarayanan. Mega-nerf: Scalable construction of large-scale nerfs for virtual fly-throughs. In Proceedings of the IEEE/CVF conference on computer vision and pattern recognition, pages 12922–12931, 2022.
- [52] Jianyuan Wang, Nikita Karaev, Christian Rupprecht, and David Novotny. Vggsfm: Visual geometry grounded deep structure from motion. In Proceedings of the IEEE/CVF conference on computer vision and pattern recognition, pages 21686–21697, 2024.
- [53] Jianyuan Wang, Minghao Chen, Nikita Karaev, Andrea Vedaldi, Christian Rupprecht, and David Novotny. Vggt: Visual geometry grounded transformer. arXiv preprint arXiv:2503.11651, 2025.

- [54] Qianqian Wang, Vickie Ye, Hang Gao, Weijia Zeng, Jake Austin, Zhengqi Li, and Angjoo Kanazawa. Shape of motion: 4d reconstruction from a single video. 2024.
- [55] Qianqian Wang, Yifei Zhang, Aleksander Holynski, Alexei A Efros, and Angjoo Kanazawa. Continuous 3d perception model with persistent state. *arXiv preprint arXiv:2501.12387*, 2025.
- [56] Shuzhe Wang, Vincent Leroy, Johann Cabon, Boris Chidlovskii, and Jerome Revaud. Dust3r: Geometric 3d vision made easy. In *Proceedings of the IEEE/CVF Conference on Computer Vision and Pattern Recognition*, pages 20697–20709, 2024.
- [57] Zhou Wang, Alan C Bovik, Hamid R Sheikh, and Eero P Simoncelli. Image quality assessment: from error visibility to structural similarity. *IEEE transactions on image processing*, 13(4):600–612, 2004.
- [58] Xingkui Wei, Yinda Zhang, Zhuwen Li, Yanwei Fu, and Xiangyang Xue. Deepsfm: Structure from motion via deep bundle adjustment. In *Computer Vision—ECCV 2020: 16th European Conference, Glasgow, UK, August 23–28, 2020, Proceedings, Part I 16*, pages 230–247. Springer, 2020.
- [59] Changchang Wu. Towards linear-time incremental structure from motion. In *2013 International Conference on 3D Vision-3DV 2013*, pages 127–134. IEEE, 2013.
- [60] Guanjun Wu, Taoran Yi, Jiemin Fang, Lingxi Xie, Xiaopeng Zhang, Wei Wei, Wenyu Liu, Qi Tian, and Xinggang Wang. 4d gaussian splatting for real-time dynamic scene rendering. In *Proceedings of the IEEE/CVF conference on computer vision and pattern recognition*, pages 20310–20320, 2024.
- [61] Haofei Xu, Jing Zhang, Jianfei Cai, Hamid Rezaatofghi, and Dacheng Tao. Gmflow: Learning optical flow via global matching. In *Proceedings of the IEEE/CVF conference on computer vision and pattern recognition*, pages 8121–8130, 2022.
- [62] Yufei Xu, Jing Zhang, Qiming Zhang, and Dacheng Tao. Vitpose: Simple vision transformer baselines for human pose estimation. *Advances in neural information processing systems*, 35:38571–38584, 2022.
- [63] Zhen Xu, Sida Peng, Haotong Lin, Guangzhao He, Jiaming Sun, Yujun Shen, Hujun Bao, and Xiaowei Zhou. 4k4d: Real-time 4d view synthesis at 4k resolution. In *CVPR*, 2024.
- [64] Jinyu Yang, Mingqi Gao, Zhe Li, Shang Gao, Fangjing Wang, and Feng Zheng. Track anything: Segment anything meets videos. *arXiv preprint arXiv:2304.11968*, 2023.
- [65] Lihe Yang, Bingyi Kang, Zilong Huang, Xiaogang Xu, Jiashi Feng, and Hengshuang Zhao. Depth anything: Unleashing the power of large-scale unlabeled data. In *Proceedings of the IEEE/CVF Conference on Computer Vision and Pattern Recognition*, pages 10371–10381, 2024.
- [66] Zeyu Yang, Hongye Yang, Zijie Pan, and Li Zhang. Real-time photorealistic dynamic scene representation and rendering with 4d gaussian splatting. *arXiv preprint arXiv:2310.10642*, 2023.
- [67] Ziyi Yang, Xinyu Gao, Wen Zhou, Shaohui Jiao, Yuqing Zhang, and Xiaogang Jin. Deformable 3d gaussians for high-fidelity monocular dynamic scene reconstruction. In *Proceedings of the IEEE/CVF conference on computer vision and pattern recognition*, pages 20331–20341, 2024.
- [68] Yao Yao, Zixin Luo, Shiwei Li, Tian Fang, and Long Quan. Mvsnet: Depth inference for unstructured multi-view stereo. In *Proceedings of the European conference on computer vision (ECCV)*, pages 767–783, 2018.
- [69] Zongxin Ye, Wenyu Li, Sidun Liu, Peng Qiao, and Yong Dou. Absgs: Recovering fine details in 3d gaussian splatting. In *Proceedings of the 32nd ACM International Conference on Multimedia*, pages 1053–1061, 2024.
- [70] Zehao Yu and Shenghua Gao. Fast-mvsnet: Sparse-to-dense multi-view stereo with learned propagation and gauss-newton refinement. In *Proceedings of the IEEE/CVF conference on computer vision and pattern recognition*, pages 1949–1958, 2020.
- [71] Jingyang Zhang, Shiwei Li, Zixin Luo, Tian Fang, and Yao Yao. Vis-mvsnet: Visibility-aware multi-view stereo network. *International Journal of Computer Vision*, 131(1):199–214, 2023.
- [72] Junyi Zhang, Charles Herrmann, Junhwa Hur, Varun Jampani, Trevor Darrell, Forrester Cole, Deqing Sun, and Ming-Hsuan Yang. Monst3r: A simple approach for estimating geometry in the presence of motion. *arXiv preprint arXiv:2410.03825*, 2024.
- [73] Richard Zhang, Phillip Isola, Alexei A Efros, Eli Shechtman, and Oliver Wang. The unreasonable effectiveness of deep features as a perceptual metric. In *Proceedings of the IEEE conference on computer vision and pattern recognition*, pages 586–595, 2018.

- [74] Zhoutong Zhang, Forrester Cole, Zhengqi Li, Michael Rubinstein, Noah Snavely, and William T Freeman. Structure and motion from casual videos. In *European Conference on Computer Vision*, pages 20–37. Springer, 2022.
- [75] Chengwei Zheng, Lixin Xue, Juan Zarate, and Jie Song. Gstar: Gaussian surface tracking and reconstruction. *arXiv preprint arXiv:2501.10283*, 2025.
- [76] Jiaxuan Zhu and Hao Tang. Dynamic scene reconstruction: Recent advance in real-time rendering and streaming. *arXiv preprint arXiv:2503.08166*, 2025.
- [77] Ruijie Zhu, Yanzhe Liang, Hanzhi Chang, Jiacheng Deng, Jiahao Lu, Wenfei Yang, Tianzhu Zhang, and Yongdong Zhang. Motiongs: Exploring explicit motion guidance for deformable 3d gaussian splatting. *Advances in Neural Information Processing Systems*, 37:101790–101817, 2024.
- [78] Yingying Zhu, Dong Huang, Fernando De La Torre, and Simon Lucey. Complex non-rigid motion 3d reconstruction by union of subspaces. In *Proceedings of the IEEE conference on computer vision and pattern recognition*, pages 1542–1549, 2014.
- [79] Michael Zollhöfer, Matthias Nießner, Shahram Izadi, Christoph Rehmann, Christopher Zach, Matthew Fisher, Chenglei Wu, Andrew Fitzgibbon, Charles Loop, Christian Theobalt, et al. Real-time non-rigid reconstruction using an rgb-d camera. *ACM Transactions on Graphics (ToG)*, 33(4):1–12, 2014.
- [80] Matthias Zwicker, Hanspeter Pfister, Jeroen Van Baar, and Markus Gross. Ewa splatting. *IEEE Transactions on Visualization and Computer Graphics*, 8(3):223–238, 2002.

## A Dataset & Training Details

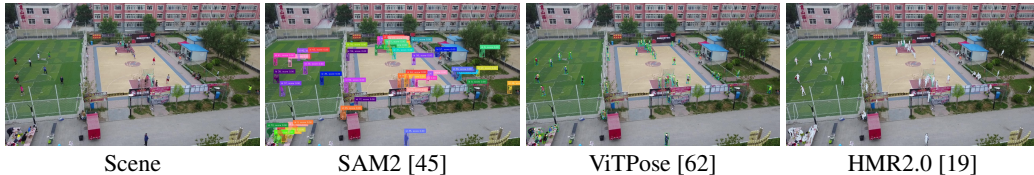


Figure 8: **Visual Examples of Initial Estimates.** Each initial estimate is used as input for the subsequent human-scene reconstruction process.

### A.1 Dataset Details

We select four scenes from each dataset, with most scenes comprising approximately 200 images in total, including both training and test sets.

1. VisDrone: uav0013\_00000, uav0079\_00480, uav0084\_00000, uav0099\_02109
2. Manipal-UAV: 40\_GND\_P1, 40\_VGT\_P1, 50\_GND\_P1, 50\_RD\_P1
3. Okutama-Action: 1\_2\_2, 1\_2\_6, 1\_2\_8, 1\_2\_9

In the VisDrone dataset, humans have an average size of approximately  $29 \times 78$  pixels, while in the Manipal-UAV dataset, the average size is around  $7 \times 17$  pixels. In the Okutama dataset, humans typically appear at an average size of  $17 \times 44$  pixels.

### A.2 Training Details

**Initialization** Figure 8 presents visual examples of human masks generated by SAM2 [45], 2D keypoint poses estimated by ViTPose [62], and human meshes reconstructed by HMR2.0 [19]. We observe that human bounding boxes are generally more reliable than the reconstructed human mesh parameters. Therefore, we set  $\eta_{box}$  to 1.2 to filter out erroneous projected human meshes in image space that appear excessively large compared to their corresponding bounding boxes.

**Joint Human-Scene Reconstruction** To reconstruct the background mesh, we first filter point maps based on confidence scores. The confidence threshold  $\eta_{conf}$  is determined according to the UAV’s altitude. Specifically, we set  $\eta_{conf}$  to 5 for the Manipal-UAV dataset, 20 for Okutama-Action, and 40 for the VisDrone dataset. For high-altitude captures (e.g., 40–50 meters), a lower confidence threshold is used since most point maps correspond to static background. In contrast, for low-altitude scenarios, a higher confidence threshold is applied to exclude point maps from dynamic regions. For scale optimization, we first initialize the scale  $\sigma$  to 40. We then select approximately 5–10 human instances and sample 5 frames at intervals of 5 frames. Keypoints corresponding to the main body



are used for optimization. We set the learning rate  $\alpha$  to 0.1 and perform  $T_{opt}$  to 30 optimization steps. We note that the root translation is typically associated with the pelvis joint. To convert the ground contact point to the root translation, we apply a vertical offset of 1 unit.

**3D Gaussian Scen Modeling** To optimize all Gaussians, we use various loss functions and regularizations in Eq. (5) in the main paper. The opacity regularization  $L_o$  is defined as

$$L_o = \sum -o_{all} \log(o_{all}) - \sum m_{sky} \log(1 - o_{all}) \quad (6)$$

where  $o_{all}$  is the rendered opacity map from all Gaussian attributes and  $m_{sky}$  is the sky mask. Most of the UAV scenes selected do not include sky regions. Only two scenes—uav0013\_00000 and uav0099\_02109 from the VisDrone dataset—contain visible sky areas. The remaining ten scenes exclude sky regions from consideration.

Following GART [30] and OmniRe [9],  $L_{smpl}$  includes KNN regularization  $L_{knn}$  and temporal smoothness regularization  $L_{smooth}$ . We apply KNN regularization for all Gaussian attributes to constrain the transformation and appearance of neighbors in order to reduce the artifacts.

$$L_{knn} = \sum_{(\mu, r, s, c, o) \in g_h} \lambda_{knn} STD_{i \in KNN(\mu_i)}(\mu_i, r_i, s_i, c_i, o_i), \quad (7)$$

where  $STD$  denotes the standard deviation. Furthermore, we apply temporal smoothness regularization to ensure that human body poses  $\theta_t$  vary smoothly over time by encouraging consistency between the current pose and its adjacent frames,

$$L_{smooth} = 0.5 \lambda_{smooth} \|(\theta_t - \theta_{t-1}) + (\theta_t - \theta_{t+1})\|. \quad (8)$$

We set  $\lambda_{pho}$  to 0.2,  $\lambda_o$  to 0.05,  $\lambda_{knn}$  to 0.01,  $\lambda_{smooth}$  to 0.001. We optimize all Gaussian attributes and all SMPL parameters using Adam optimizer for 30,000 iterations. For optimizing background Gaussian attributes, we set the learning rates for rotations, scales, zeroth-order spherical harmonics, the remaining spherical harmonics to 0.001, 0.005, 0.0025, and 0.000125 respectively. To optimize the human Gaussian attributes, we set the learning rates for rotations, scales, zeroth-order spherical harmonics, and higher-order spherical harmonics to 0.0016, 0.005, 0.0025, and 0.000125, respectively. For human pose parameters, the learning rates for rotation and translation are set to 0.00001 and 0.0005, respectively. For densification for Gaussian attributes, we utilize the strategy of AbsGS [69]. The densification threshold for the position gradient is set to 0.0003.

## B Experimental Results

### B.1 Zoom-in Human Regions

Fig. 9 shows example visualizations of human regions, comparing our method with the ground truth images. In the VisDrone dataset, human figures are approximately  $30 \times 79$  pixels in size, while in the Okutama-Action dataset, they are around  $17 \times 44$  pixels.

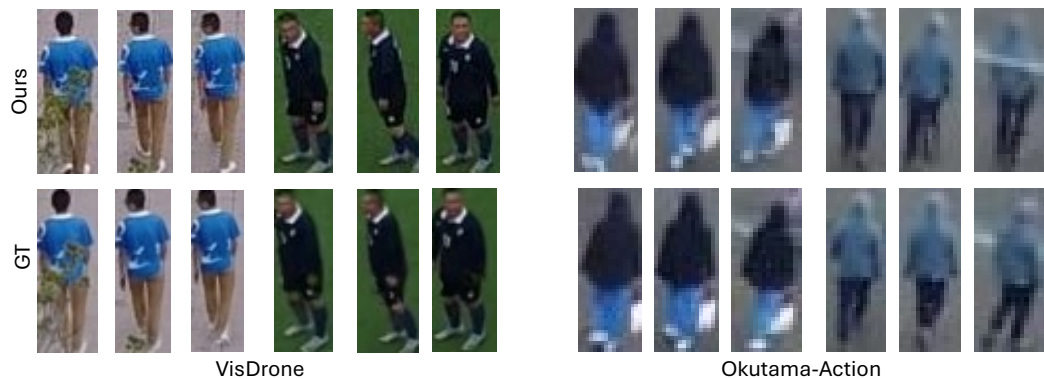


Figure 9: Visual Examples of Zoom-in Human Regions on VisDrone and Okutama-Action Datasets

## B.2 Per-scene Breakdown

To supplement Table 1 of the main paper, we present per-scene experimental results in terms of PSNR, SSIM, and LPIPS, as shown in Table 4, 6, and 8. Table 5, 7 and 9 provide a breakdown of image quality metrics focused on human-only regions, complementing the results in Table 2 of the main paper.

**VisDrone Dataset** Additionally, we provide a detailed breakdown of the ablation study results to complement Table 3.

Table 4: **Breakdown results on the VisDrone dataset** [7]. Red, orange, and yellow indicate the first, second, and third best performing algorithms for each metric.

Method	uav0013_00000			uav0079_00480			uav0084_00000			uav0099_02109			Mean		
	PSNR $\uparrow$	SSIM $\uparrow$	LPIPS $\downarrow$	PSNR $\uparrow$	SSIM $\uparrow$	LPIPS $\downarrow$	PSNR $\uparrow$	SSIM $\uparrow$	LPIPS $\downarrow$	PSNR $\uparrow$	SSIM $\uparrow$	LPIPS $\downarrow$	PSNR $\uparrow$	SSIM $\uparrow$	LPIPS $\downarrow$
TK-Planes [39]	27.10	0.747	0.398	22.36	0.614	0.493	25.30	0.788	0.338	21.17	0.427	0.569	23.98	0.644	0.450
3DGS [26]	27.21	0.833	0.211	24.57	0.779	0.214	23.21	0.861	0.180	23.38	0.655	0.274	24.59	0.782	0.220
4DGS [67]	26.74	0.761	0.401	18.27	0.507	0.546	26.40	0.885	0.208	18.90	0.358	0.603	22.58	0.628	0.440
DeformableGS [60]	12.66	0.522	0.667	13.72	0.477	0.691	21.22	0.757	0.376	14.22	0.330	0.724	15.46	0.522	0.614
UAV4D (Ours)	28.13	0.847	0.149	25.52	0.801	0.137	26.82	0.886	0.074	23.66	0.665	0.227	26.03	0.800	0.147
Ours wo SMPL	25.85	0.775	0.161	24.70	0.765	0.232	23.59	0.870	0.199	23.21	0.642	0.258	24.33	0.763	0.212
Ours wo Scale	26.43	0.785	0.151	17.49	0.493	0.549	26.49	0.787	0.140	21.70	0.539	0.174	23.02	0.651	0.254
Ours wo Refine	27.56	0.792	0.192	25.50	0.801	0.136	26.81	0.886	0.074	23.32	0.612	0.260	25.79	0.772	0.165

Table 5: **Breakdown results on the VisDrone dataset** [7], focusing on **human-only** regions. Red, orange, and yellow indicate the first, second, and third best performing algorithms for each metric.

Method	uav0013_00000		uav0079_00480		uav0084_00000		uav0099_02109		Mean	
	PSNR $\uparrow$	SSIM $\uparrow$	PSNR $\uparrow$	SSIM $\uparrow$	PSNR $\uparrow$	SSIM $\uparrow$	PSNR $\uparrow$	SSIM $\uparrow$	PSNR $\uparrow$	SSIM $\uparrow$
TK-Planes [39]	18.54	0.586	17.28	0.453	18.66	0.560	16.10	0.579	17.65	0.544
3DGS [26]	18.72	0.640	17.50	0.512	16.81	0.565	13.01	0.474	16.51	0.548
4DGS [67]	17.32	0.538	14.61	0.372	20.43	0.675	12.65	0.455	16.25	0.510
DeformableGS [60]	12.06	0.295	11.23	0.248	15.47	0.476	11.59	0.395	12.59	0.354
UAV4D (Ours)	19.07	0.672	17.82	0.525	18.79	0.629	16.24	0.590	17.98	0.604

Table 6: **Breakdown results on the Okutama-Action dataset** [3]. Red, orange, and yellow indicate the first, second, and third best performing algorithms for each metric

Method	1_2_2			1_2_6			1_2_8			1_2_9			Mean		
	PSNR $\uparrow$	SSIM $\uparrow$	LPIPS $\downarrow$	PSNR $\uparrow$	SSIM $\uparrow$	LPIPS $\downarrow$	PSNR $\uparrow$	SSIM $\uparrow$	LPIPS $\downarrow$	PSNR $\uparrow$	SSIM $\uparrow$	LPIPS $\downarrow$	PSNR $\uparrow$	SSIM $\uparrow$	LPIPS $\downarrow$
TK-Planes [39]	30.63	0.808	0.369	24.43	0.634	0.393	31.89	0.829	0.384	24.97	0.601	0.438	27.98	0.718	0.396
3DGS [26]	30.90	0.869	0.168	25.79	0.796	0.139	33.34	0.913	0.182	27.83	0.847	0.109	29.46	0.856	0.150
4DGS [67]	33.16	0.869	0.291	28.33	0.844	0.181	33.60	0.879	0.294	28.38	0.780	0.245	30.87	0.843	0.253
DeformableGS [60]	34.51	0.945	0.077	28.49	0.897	0.096	35.74	0.948	0.089	26.15	0.788	0.196	31.22	0.894	0.114
UAV4D (Ours)	31.76	0.897	0.105	26.57	0.844	0.100	35.96	0.947	0.075	29.49	0.901	0.056	30.94	0.897	0.084

Table 7: **Breakdown results on the Okutama-Action dataset** [3], focusing on **human-only** regions. Red, orange, and yellow indicate the first, second, and third best performing algorithms for each metric.

Method	1_2_2		1_2_6		1_2_8		1_2_9		Mean	
	PSNR $\uparrow$	SSIM $\uparrow$	PSNR $\uparrow$	SSIM $\uparrow$	PSNR $\uparrow$	SSIM $\uparrow$	PSNR $\uparrow$	SSIM $\uparrow$	PSNR $\uparrow$	SSIM $\uparrow$
TK-Planes [39]	18.94	0.635	20.91	0.671	18.34	0.667	18.39	0.550	19.14	0.631
3DGS [26]	19.97	0.714	21.05	0.701	18.76	0.694	16.50	0.513	19.07	0.656
4DGS [67]	15.80	0.504	22.28	0.735	19.65	0.725	14.99	0.446	18.18	0.602
DeformableGS [60]	19.52	0.702	13.43	0.505	15.51	0.565	16.86	0.514	16.33	0.571
Our Method	19.01	0.667	21.07	0.704	19.70	0.734	18.19	0.549	19.49	0.664

Table 8: **Breakdown results on the Manipal-UAV dataset** [2]. Red, orange, and yellow indicate the first, second, and third best performing algorithms for each metric

Method	40_GND_P1			40_VGT_P1			50_GND_P1			50_RD_P1			Mean		
	PSNR $\uparrow$	SSIM $\uparrow$	LPIPS $\downarrow$	PSNR $\uparrow$	SSIM $\uparrow$	LPIPS $\downarrow$	PSNR $\uparrow$	SSIM $\uparrow$	LPIPS $\downarrow$	PSNR $\uparrow$	SSIM $\uparrow$	LPIPS $\downarrow$	PSNR $\uparrow$	SSIM $\uparrow$	LPIPS $\downarrow$
TK-Planes [39]	28.09	0.842	0.383	26.88	0.732	0.427	27.59	0.823	0.364	29.63	0.788	0.494	28.05	0.796	0.417
3DGS [26]	31.02	0.907	0.204	27.54	0.807	0.234	30.32	0.911	0.191	30.72	0.845	0.283	29.90	0.867	0.228
4DGS [67]	21.27	0.710	0.503	27.99	0.796	0.318	31.00	0.910	0.248	23.34	0.705	0.569	25.90	0.780	0.410
DeformableGS [60]	31.28	0.915	0.251	13.10	0.564	0.624	16.04	0.687	0.536	30.13	0.827	0.361	22.64	0.748	0.443
UAV4D (Ours)	31.34	0.917	0.181	27.88	0.814	0.191	30.86	0.919	0.143	31.36	0.849	0.219	30.36	0.875	0.184

Table 9: **Breakdown results on the Manipal-UAV dataset** [2], focusing on **human-only** regions. Red, orange, and yellow indicate the first, second, and third best performing algorithms for each metric.

Method	40_GND_P1		40_VGT_P1		50_GND_P1		50_RD_P1		Mean	
	PSNR $\uparrow$	SSIM $\uparrow$	PSNR $\uparrow$	SSIM $\uparrow$	PSNR $\uparrow$	SSIM $\uparrow$	PSNR $\uparrow$	SSIM $\uparrow$	PSNR $\uparrow$	SSIM $\uparrow$
TK-Planes [39]	20.52	0.838	15.79	0.577	19.11	0.822	18.11	0.769	18.38	0.752
3DGS [26]	19.35	0.816	15.45	0.587	18.55	0.798	18.60	0.791	17.99	0.748
4DGS [67]	21.41	0.845	15.83	0.603	20.98	0.850	18.68	0.783	19.23	0.770
DeformableGS [60]	20.66	0.837	15.64	0.597	20.27	0.843	18.05	0.771	18.65	0.762
Our Method	21.92	0.880	15.61	0.594	21.24	0.872	18.76	0.792	19.38	0.784

### B.3 Visual Comparison

Figure 10 presents the remaining scenes not included in the main paper due to space limitations. Additionally, we provide a project website at <https://uav4d.github.io/>, which contains rendering videos for all scenes.

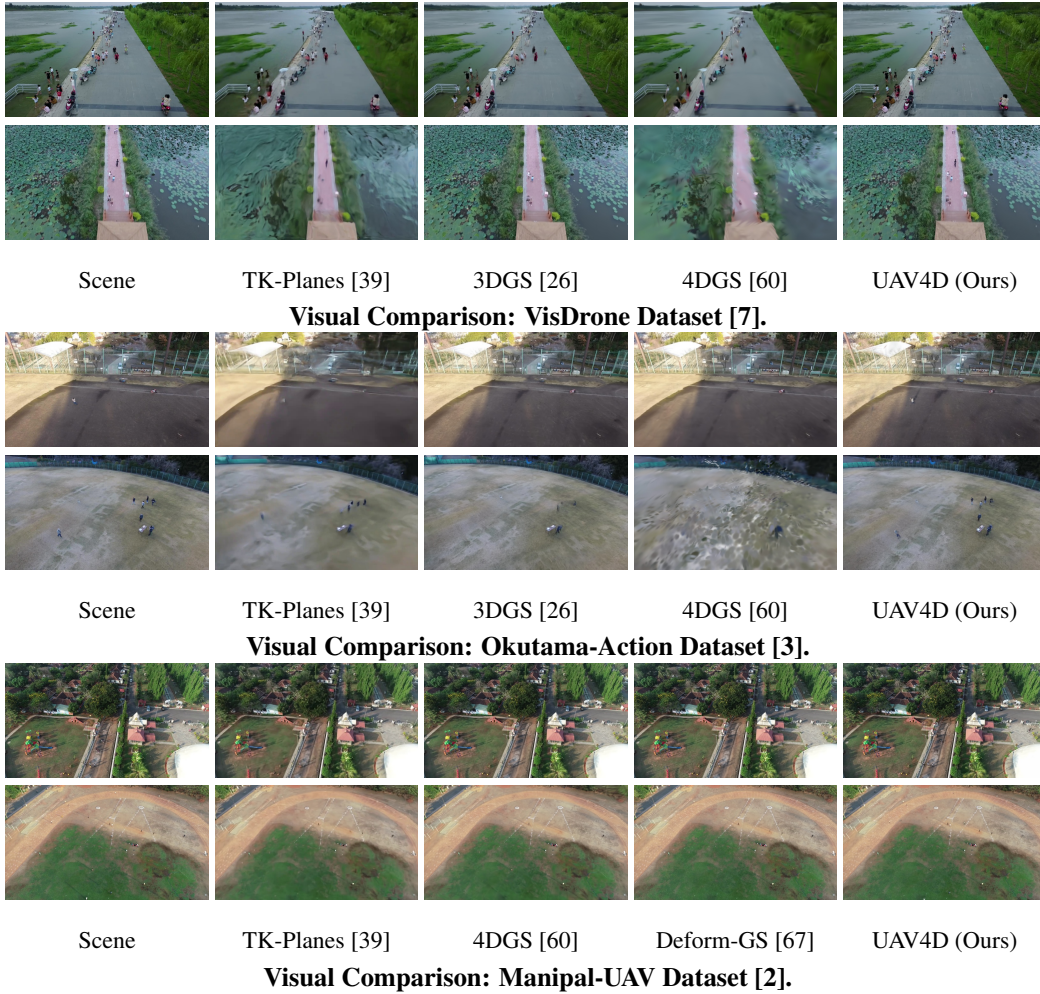


Figure 10: **Visual Comparisons across UAV Datasets.** Rendering comparisons on VisDrone [7], Okutama-Action [3], and Manipal-UAV [2]. Our method consistently outperforms other baselines in handling dynamic scenes with small, moving humans.